Journal of Electron Spectroscopy and Related Phenomena 241 (2020) 146837

Contents lists available at ScienceDirect

Journal of Electron Spectroscopy and Related Phenomena

journal homepage: www.elsevier.com/locate/elspec

Field emission properties of single crystalline W_5O_{14} and $W_{18}O_{49}$ nanowires

Muhammad Saqib[a], Janez Jelenc[a], Luka Pirker[a], Srečo D. Škapin[a], Lorenzo De Pietro[b], Urs Ramsperger[b], Alexandr Knápek[c], Ilona Müllerová[c], Maja Remškar[a,*]

[a] Jozef Stefan Institute, Condensed Matter Physics Department, Ljubljana, Slovenia
[b] ETH Zurich, Department of Physics, Zurich, Switzerland
[c] Institute of Scientific Instruments, Czech Academy of Sciences, Brno, Czech Republic

ARTICLE INFO

Keywords:
Nanowires
Tungsten oxides
Electron emitter
Field enhancement factor
Work function

ABSTRACT

Single crystalline tungsten oxides in a form of W_5O_{14} and $W_{18}O_{49}$ nanowires were synthesized by iodine transport method. The morphology, work functions and field emission properties of these nanowires were investigated. Work functions of the W_5O_{14} (4.20–4.34 eV) and $W_{18}O_{49}$ (4.55–4.57 eV) nanowires (NWs) have been measured by Kelvin probe force microscopy (KPFM) in ultra-high vacuum. Field emission (FE) measurements of individual nanowires were performed in ultra-high vacuum at microscopic and macroscopic distances between the emitter and electron collector. The obtained FE curves at microscopic distances were analyzed in the framework of the Fowler–Nordheim (F–N) theory. Field enhancement factors of W_5O_{14} at the emitter-collector distance of 2, 4 and 5 μm were calculated to be 110 ± 10, 180 ± 25 and 210 ± 30, respectively, and 125 ± 15 for W18O49 at 2 μm. At macroscopic distances, the F–N theory revealed unrealistic high field enhancement factors: for W_5O_{14} at 1 mm it was 17,000 ± 500, and for $W_{18}O_{49}$, the field enhancement factors were 5050 ± 30 and 6450 ± 30 at 600 μm and 800 μm emitter-collector distance, respectively. Therefore, more realistic model was discussed. The lower work function and typically smaller diameter of the W_5O_{14} nanowires in comparison with the $W_{18}O_{49}$ wires, range the W_5O_{14} nanowires to the promising sources of electrons in field emission devices.

1. Introduction

Metal oxides are the key components for the development of many advanced functional materials and smart devices. Among them are tungsten oxides, which belong to a family of transition metal oxides, and have various applications in photocatalysis [1], electrochemistry [2], energy conversion [2], gas sensors [3], and as recently found also in phototherapy [4]. Besides stoichiometric WO_3, which exists at different temperatures in several structures, such as monoclinic, triclinic, tetragonal, orthorhombic, cubic and hexagonal [5], oxygen reduced WO_{3-x} phases are also known, where tungsten oxidation state for some atoms changes from W^{6+} to W^{5+}. Among these phases, $W_{18}O_{49}$ is the most reduced stable phase. Less reduced W_5O_{14} crystals in needle like shape were reported as a homogeneous phase using iron in 1978 [6] and nickel in 2007 [7] as growth promoters. Oxygen vacancies in these sub-stoichiometric WO_{3-x} phases create donor states and strongly improve the electrical conductivity. Besides, these defects preferentially accumulate at the formed crystallographic shear planes. Here they change corner-shared octahedra WO_6 of stoichiometric WO_3 to edge-shared or face-shared WO_6 octahedra and bonds are formed between W^{+5} ions in edge sharing pairs [8]. In contrary with the stoichiometric WO_3 semiconductor with a band gap in the range of 2.5–3.2 eV [9] and electrical conductance from 10 to 10^4 Ωcm [10,11], the reduced W_5O_{14} phase growing as nanowires, revealed metallic conductivity with an electrical resistance of 25 μΩcm [7]. For comparison, electrical resistance of the most reduced $W_{18}O_{49}$ wires is 2750 μΩcm [12], i.e. more than two orders of magnitude larger with respect to W_5O_{14}.

Over the last few years, field emission (FE) studies have been performed with different phases of WO_{3-x}, mainly focused on $W_{18}O_{49}$ NWs [13,14] arrays, where FE properties with a low threshold field of 4.37 V/μm for an FE current density of 10 mA/cm^2 were measured, as well as a high time stability of FE current [14]. FE studies performed with thermally evaporated $W_{18}O_{49}$ NWs depended on temperature and anomalous changes in emission current were found in temperature range 300 K–723 K [13]. Decreasing of FE currents under the same applied electrical field with decreasing the temperature from RT to 143 K, was explained with the phonon-assisted tunnelling of electrons from defect states to the conduction band [15]. In a case of W_5O_{14} NWs, in-situ FE measurement was performed using FE-TEM holder, where a current as high as 35 μA was extracted from a single NW in parallel

* Corresponding author.
E-mail address: maja.remskar@ijs.si (M. Remškar).

https://doi.org/10.1016/j.elspec.2019.03.005
Received 13 August 2018; Received in revised form 18 February 2019; Accepted 12 March 2019
Available online 15 March 2019
0368-2048/

orientation to the electric field of 160 V/μm [16]. The second experiment was performed on a film composed of W_5O_{14} NWs that were oriented perpendicular to the electric field. The emitting current densities up to 6.4 mA/cm^2 have been obtained at a very low electric field of about 3 V/μm. The NWs were emitting for 100 h, with the emitting current stabilizing after 40 h at 2.4 μA [17].

In the present study, we report a comparative study of surface and field emission properties of W_5O_{14} and $W_{18}O_{49}$ NWs synthesized by a modified method using WO_3 and elemental tungsten as starting materials in the iodine transport reaction. Detailed structural and surface properties were revealed using X-ray-diffraction (XRD), scanning tunnelling microscopy (STM) and scanning electron microscopy (SEM). Work functions of single NWs were measured with Kelvin probe force microscopy (KPFM). The FE properties of individual NWs were measured at multiple distances that are orders of magnitude apart (2–5 μm and approx. 1 mm).

2. Materials and methods

The W_5O_{14} (O/W = 2.8) NWs were synthesized by iodine transport method [7] using nickel as a growth promoter and WO_3 as a source of tungsten and oxygen. The starting material consisted of 352.7 mg of WO_3 powder (Sigma Aldrich, 99.99%), 37.5 mg nickel (metal foil) and 567 mg iodine (1–3 mm beads, Sigma Aldrich, 99.7%). Adding a small quantity of tungsten powder (20 mg), growth of the $W_{18}O_{49}$ (O/W = 2.72) NWs was promoted. Evacuated (4×10^{-6} mbar) and sealed quartz ampoules were inserted into a two-zone furnace in such a way, that the material was transported from 860 °C to 736 °C. Transport reaction ran for 500 h and then the ampules were cooled with 70 °C/hour cooling rate. The transported materials of light (W_5O_{14}) and deep blue ($W_{18}O_{49}$) colour were obtained. Both W_5O_{14} and $W_{18}O_{49}$ consist of long, rigid NWs which tend to clump into bundles.

The crystalline structure of the NWs was examined by XRD at room temperature with D4 Endeavor diffractometer (Bruker AXS) using a quartz monochromatic Cu Kα1 radiation source (λ = 0.1541 nm) and a Sol-X dispersive detector. Morphology, surface structure and work functions of W_5O_{14} and $W_{18}O_{49}$ NWs were measured by scanning electron microscope (SEM) Supra 36 V P, Carl Zeiss, scanning tunneling microscope (STM), atomic force microscope (AFM), and Kelvin probe operating in ultra-high vacuum (Omicron VT-AFM).

The FE properties of individual W_5O_{14} NWs or $W_{18}O_{49}$ wires and NWs were measured in microscopic and macroscopic regimes. The NWs were attached on tungsten electrochemically etched tips by using OmniProbe Nano-manipulator in a Helios NanoLab 650 Focused Ion Beam-scanning electron microscope (FIB). At microscopic distances, the FE measurements were performed in ultra-high vacuum (Omicron VT-AFM) using a diode configuration, with a negatively biased WO_{3-x} wire as an electron source (cathode) and a freshly cleaved HOPG as an electron collector (anode). In the macroscopic regime, both nanowires were tested in slightly different configuration, which should not affect the results. While the FE testing of a W_5O_{14} NW was performed with positively biased electron extractor [18], the $W_{18}O_{49}$ NW was tested with negatively biased cathode and grounded anode [19].

3. Results

3.1. Morphology and crystal structure studies

Electron microscopy images (Fig. 1) of (a) W_5O_{14} and (b) $W_{18}O_{49}$ wires show that the length of both types of NWs exceeds several ten μm. The nanowires are very rigid and have a homogeneous diameter along their length. The mean diameter of the W_5O_{14} NWs is in the range of 100–200 nm, while majority of the $W_{18}O_{49}$ wires are thicker (up to 3 μm) with rare thinner ones.

The XRD spectra (Fig. 2) of (a) W_5O_{14} and (b) $W_{18}O_{49}$ match the tetragonal W_5O_{14} structure (JCPDS 71-0292) with lattice parameter: a = 23.33 Å and c = 3.78 Å, and monoclinic $W_{18}O_{49}$ phase with lattice parameters: a = 18.32 Å, b = 3.78 Å, c = 14.03 Å and β = 115.20° (JCPDS 036-0101) [20], respectively. Since the NWs have preferential orientation parallel with the substrate, the relative intensities differ from the ones in the database. In particular, the (001) peak of W_5O_{14} and the (010) peak of $W_{18}O_{49}$ which have the maximum intensity in the database, are relatively weak, while those attributed to the (hk0) interlayer distances are intensified. There are no indications of any other WO_{3-x} phase in the samples. The sharps peaks in the XRD pattern are clear evidence of high crystallinity of the materials.

High-resolution TEM images shown in the Fig. 3 reveal that both types of wires are single crystalline. While the W_5O_{14} NW (Fig. 3a) grows along [001], the $W_{18}O_{49}$ wire (Fig. 3b) grows along [010] direction [7,21]. Longitudinal axes of the growth are presented by arrows. A periodicity of 11.7 Å perpendicularly to the W_5O_{14} NW axis corresponds to the (200) planes, while periodicity along the axis reveals (001) planes. In the $W_{18}O_{49}$ wires, the spacing between the $(\bar{4}03)$ planes parallel with the longitudinal axis is 3.9 ± 0.1 Å and between the (010) planes is 3.9 ± 0.1 Å. Layers, where 3-layers blocks are shifted for a half of unit cell along [010] in the monoclinic $W_{18}O_{49}$ wires, is marked with horizontal black lines.

3.2. Scanning tunnelling microscopy

Scanning tunneling microscopy (STM) was used to study the surface corrugation of the NWs, and structure of their longitudinal ends (Fig. 4). Surface corrugations on a W_5O_{14} NW are typically several nm deep and have a periodicity of 20–30 nm (Fig. 4a). Compared to W_5O_{14}, the corrugations in $W_{18}O_{49}$ wires are shallower with a typical periodicity of around 10 nm (Fig. 4b). The longitudinal terminations of the wires consequently differ. While the W_5O_{14} NWs terminate with dome-shaped rods with a typical diameter of 20 nm and curvature radius below 10 nm (Fig. 4c), the ends of the $W_{18}O_{49}$ wires terminate more abruptly revealing a porous structure without protuberances (Fig. 4d).

3.3. Kelvin probe force microscopy (KPFM)

Kelvin probe force microscopy was used to measure the work functions of the wires at the nanoscale. The contact potential difference (CPD) measured between the AFM tip and the sample is defined as $V_{CPD} = (\phi_{tip} - \phi_{sample})/e$ [22], where ϕ_{tip} and ϕ_{sample} denote work functions (WF) of the tip and the sample, respectively. The topography and the Kelvin image based on CPD were obtained simultaneously. We used the frequency modulated KPFM where the frequency variation Δf_0 is approximately proportional to the force gradient, which can be written as $\Delta f_0 \propto -f_0 (\partial F/\partial z) / 2k$ [23], where f_0 is the first resonance frequency of the cantilever (240 kHz) with an amplitude of approximately 10 nm, k is the cantilever spring constant (11.5 N/m) and F is the force acting on the cantilever. To measure the CPD separately from the topography, an alternating voltage $V = V_{DC} + V_{AC} \sin(\omega t)$ was applied between the tip and the sample with an amplitude $V_{AC} = 0.7$ V, and frequency $\omega = 2$ kHz. The topography is proportional to the part of the electrostatic force which is independent of ω, while the CPD is proportional to the frequency dependent electrostatic force $F_\omega \propto (V_{DC} - V_{CPD}) \sin(\omega t)$ which is detected by a lock-in amplifier. By tuning the V_{DC} in a way that F_ω is nullified, the value of the V_{CPD} is revealed. The WF of a tip strongly depends on the local tip conditions. By measuring V_{CPD} using the same AFM tip on the sample and on HOPG with a known WF value, 4.6 ± 0.05 eV [24], the influences of the tip WF variations were minimized.

Several measurements have been performed on different W_5O_{14} and $W_{18}O_{49}$ wires. The WF values obtained on W_5O_{14} single NW (Fig. 5a, b) were from 4.20 to 4.34 eV, i.e. for 260–400 meV lower than on HOPG. WF values from $W_{18}O_{49}$ wires were from 4.55 meV to 4.57 meV, only slightly lower (30–50 meV) than HOPG (Fig. 5c, d).

Work function was measured also as a function of surface

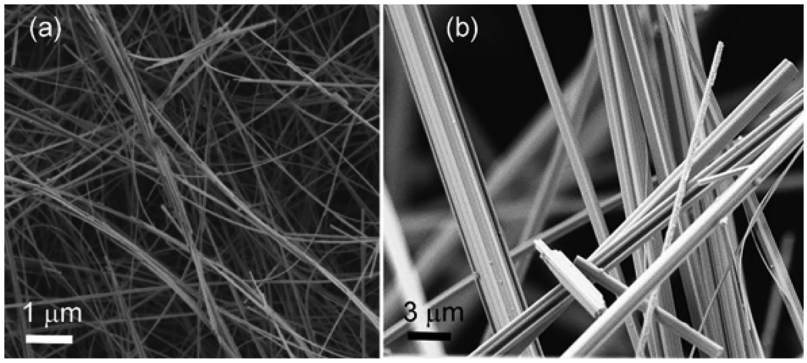

Fig. 1. SEM images of a) W_5O_{14} and b) $W_{18}O_{49}$ NWs.

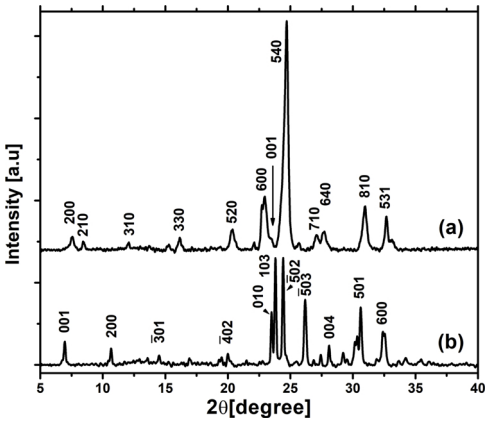

Fig. 2. The XRD spectra of a) W_5O_{14} nanowires; b) $W_{18}O_{49}$ wires.

corrugations. In the case of W_5O_{14} NWs with deep corrugations, the WF was found lower at bottom of the corrugation. In Fig. 6a, Kelvin image of a longitudinal termination of a W_5O_{14} NW is shown with two line profiles: A - perpendicular to the NW axis, and B - along the nanowire length. The minimum of the CPD in the profile A was found inside surface channels. It was 50 mV lower than on the peaks between them. At the very end of the NW, the CPD was 150 mV lower than inside the surface channels, and 400 mV lower than on HOPG (4.6 ± 0.05 eV [24]). The WF of the very end of the NW was only 4.2 eV. The reference CPD value for HOPG was taken at the ends of line profile A, where HOPG was free of any visible deformations like steps, cracks or folded layers of graphite.

Inhomogeneous electron density structure of a single W_5O_{14} NW was observed also through current enhancement in the contact-AFM current measurement (Fig. 7). Surface channels and end of the side strand (Fig. 7a) have a higher conductance than the rest of the NW (Fig. 7b). Knowing that oxygen vacancies improve electric conductivity of WO_{3-x} materials, one can conclude that they also lower the work function in the minima of the corrugations.

3.4. Field emission testing in microscopic regime

FE measurements with both kinds of wires were carried out in the STM chamber at the same distance (2 ± 0.2 μm) between a wire's apex and HOPG, which was used as an electron collector. The threshold voltages (onset voltages) for FE were determined from the minima of the corresponding Fowler–Nordheim (F–N) plots. After comparative testing, FE from a W_5O_{14} NW was studied also at a distance of 4 and 5 μm.

3.4.1. Comparative field emission studies of W_5O_{14} and $W_{18}O_{49}$ wires

The comparative FE studies were performed on two wires with very different diameters in the same FE configuration. A W_5O_{14} NW, 14 μm long and 109 nm in diameter, was attached on a tungsten wire using FIB (Fig. 8a). The NW terminated in a rectangular shape (Fig. 8b). Platinum contacts were deposited providing both a sufficient mechanical stability and electric conductance. The $W_{18}O_{49}$ wire, 247 μm in length and 4 μm in diameter, was attached on a Pt/Ir wire with silver epoxy paste (Fig. 8c). Then both tips were transferred into the UHV-STM chamber (7×10^{-10} mbar) and tested without any cleaning or annealing. A programmable voltage source (Keithley 2450) was used for applying a negative voltage onto the cathode (NW) in the range from 0 to 200 V through the field emission adapter of the Omicron STM system.

Firstly, the so-called activation process was studied, in which the FE tips were cleaned of adsorbents and/or impurities. Fig. 9 shows current-voltage (I–V) characteristics of the first (A) and the second (B) consecutive test and their corresponding F–N plots: a-b: W_5O_{14} NW, c-d: $W_{18}O_{49}$ wire. The measurements were performed at 2 μm. Significant changes have been noticed in the onset voltages in two consecutive FE measurements, which dropped for both wires in the second test. The onset voltage decreased from 63 V to 56 V for W_5O_{14} NW, and from 99 V to 74 V for $W_{18}O_{49}$ wire. A possible reason is the removal of adsorbates from the top end of the wires. Also the knees in the F–N plots of the first tests (Fig. 9a, b-A) can be explained with desorption of adsorbates under high electric fields [25]. Larger decrease of onset voltage in the case of $W_{18}O_{49}$ wire and very "noisy" FN plot for the first (A)

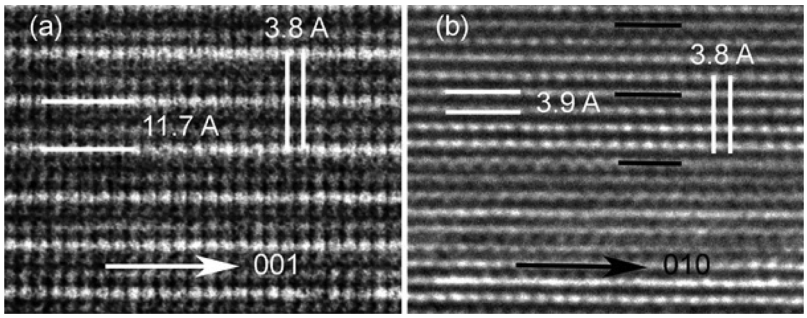

Fig. 3. High-resolution TEM: a) W_5O_{14} nanowires grown along [001] direction; b) $W_{18}O_{49}$ wires grown along [010] direction.

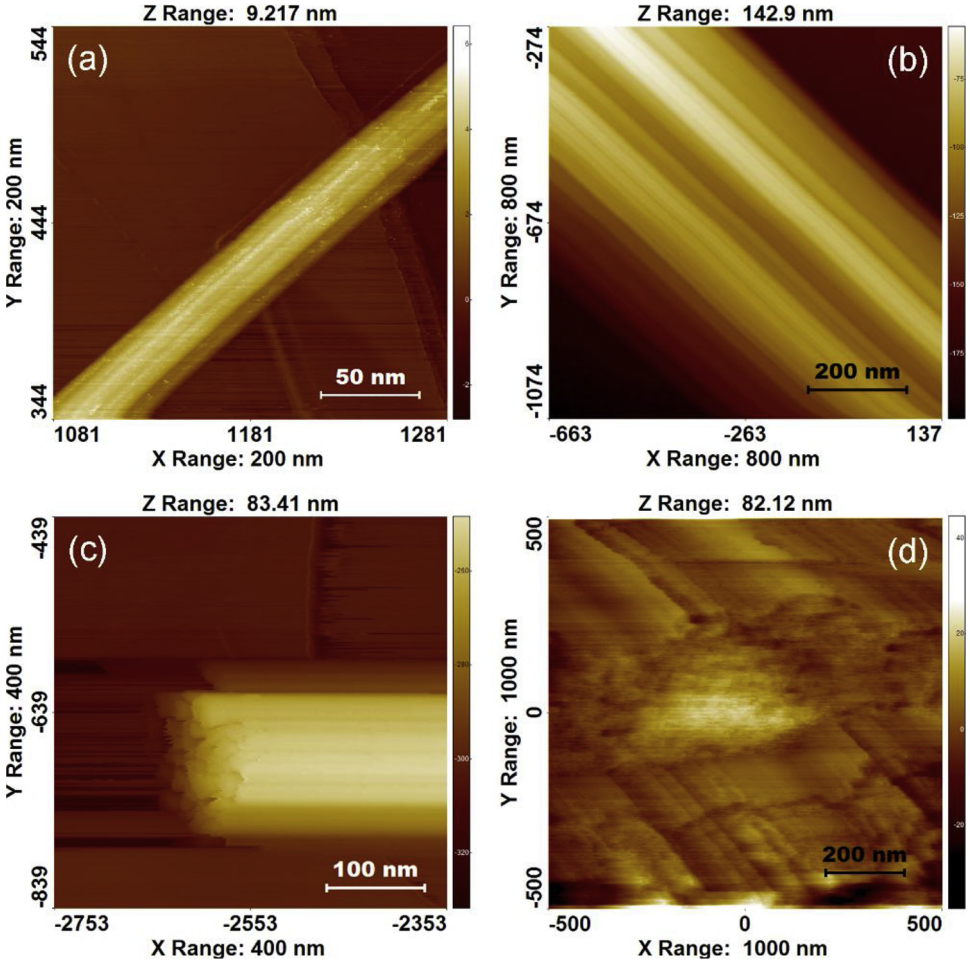

Fig. 4. STM microscopy (I = 0.3 nA; U = 0.5 V): a) single W_5O_{14} NW, 70 nm in diameter; b) a single $W_{18}O_{49}$ wire, 630 nm in diameter; c) termination of a W_5O_{14} NW, 145 nm in diameter and dome shaped protuberances; d) porous structure of a $W_{18}O_{49}$ wire.

experiment is explained with simultaneous cleaning/degradation process.

3.4.2. Field emission from the W_5O_{14} nanowire as a function of distance and time

In comparison to the $W_{18}O_{49}$ wire, the W_5O_{14} NW was found to be a more efficient field emitter because of its lower work function and lower onset voltage. Therefore, further FE tests were performed only on the W_5O_{14} NW and were carried out at three distances from HOPG: 2 µm, 4 µm and 5 µm. At each position, FE experiments were performed three times in order to confirm repeatability. No significant differences were detected when the voltage was ramped up or down. The FE current was limited to 160 nA with the aim to prevent damage of the nanowire. The onset voltages were 57 V, 67 V and 76 V at 2 µm, 4 µm and 5 µm, respectively. Fig. 10 shows the FE I–V characteristics (a) and their corresponding F–N plots (b).

In the F–N plot, a linear behaviour indicates the standard barrier-tunnelling mechanism of the field electron emission. The waviness of the F–N curves corresponding to the B (4 µm) and C (5 µm) positions cannot be explained by desorption of adsorbates, because the same FE emitter was used at all three positions and the plot A (the first test in this series) is practically linear. A possible reason for the deviation from the linearity is the electrical force which strengthens the emitter from a slightly curved shape (Fig. 8a). This effect might also be the origin of current instabilities observed during measurements of FE current over time (Fig. 11). Current over time was measured at 5 µm separation under 80 V and 85 V applied voltage in several sequences. The sample rate for the measurement illustrated in Fig. 11 was set to 10,000 readings/sec at 5½ digits and sent directly to the computer. In order to suppress the noise at the line frequency (50 Hz for most European countries), the NPLC (Number of Power Line Cycles) function was employed and set > 1, usually to 100 to achieve precise measurement accuracy. Typically, the current was stable for a certain period, then it suddenly jumped to a certain higher or lower value, which were not arbitrary. In Fig. 11a, a time stability test is shown. Four main values of the current over time are observed: 45 nA, 40 nA, 70 nA, 90 nA, and then again 40 nA, all with a standard deviation of 1 nA. Several FE current time stability measurements were recorded and fluctuations among similar values were found. A comparison of the I–V characteristics measured before and after ten current stability tests in total duration of 2.5 h (Fig. 11b), reveals a decrease of onset voltage after the stability test, from 75 V to 67 V. Deviations of the FE I–V curves from a typical exponential shape were observed only after time stability tests (Fig. 11b, curve 2). This effect indicates a structural or/and shape change of the NW. It is likely that high current densities, which for a short periods reached values up to 23 A/mm^2 (total cross section area of the NW was considered as the emission area), caused a local temperature increase, which affect the stoichiometry and accelerated the diffusion processes under the strong electric field. If comparing our results (Fig. 11a) to the previously published results illustrated by the Fig. 2 in [16], the waveform of the measured total emission current evince far stable behavior. The stability improvement is caused mainly by the decreased number of residual particles present in the ultra-high vacuum chamber comparing to the high vacuum ($P = 10^{-5}$ Pa) used in [16]. Based on equation of state, there are approx. 10^2 particles / cm^3 less in the ultra-high vacuum chamber comparing to the high vacuum

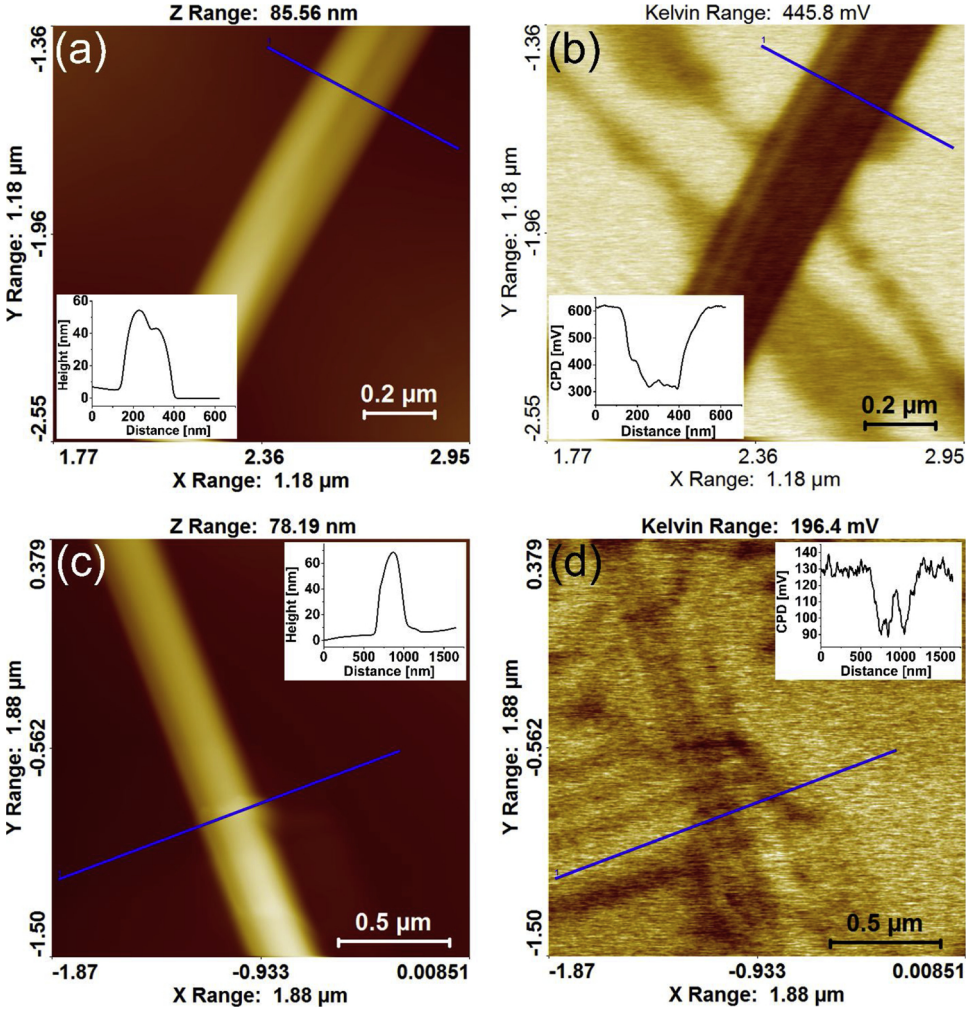

Fig. 5. AFM non contact images (df = 20 Hz) with corresponding Kelvin images: a-b: W_5O_{14}; c-d: $W_{18}O_{49}$. Line profiles marked with blue lines are shown in the insets.

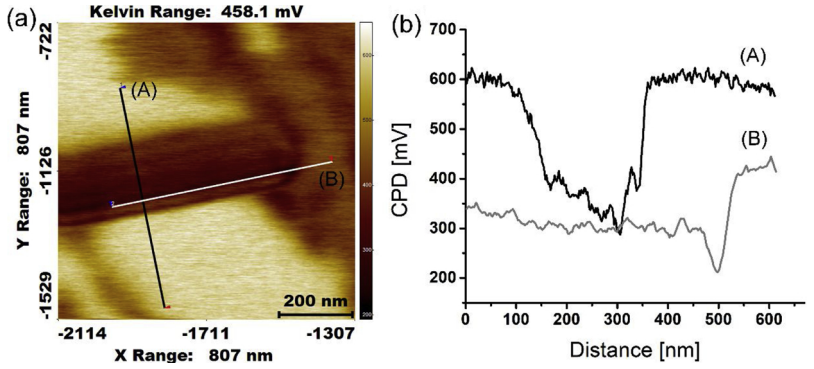

Fig. 6. Kelvin image of W_5O_{14} NW with two line profiles; b) CPD curves along A and B lines.

chamber, which reduces effects of the ions impinging on the cathode surface and hence causing ion bombardment [16]. These ions are attracted towards the cathode where they significantly influencing the thickness of the surface barrier and increasing the *1/f* and generation-recombination (g–r) noise component [18]. The effects of the ion bombardment were described by Sergeev in [32] where authors proved the relation between the ion bombardment of residual gas particles and decrease of the current noise density of the total emission current.

The local electric field at the emission point (apex) of the NWs could be much higher than the average applied field across the electrodes. As the first approximation, the field enhancement factor (β) of the local field at the apex of the NW tip was calculated using the F–N equation mimicking a parallel plate configuration and homogeneous electric field between the flat end of the nanoemitter and electron collector.

$$I = \left(A\alpha\beta^2V^2 \Big/ d^2\Phi\right) exp^{\frac{-B\Phi^{3/2}d}{\beta V}}, \quad (1)$$

where I is the emission current, $A = 1.56 \times 10^{-6}$ A V^{-2} eV and $B = 6.83 \times 10^9$ eV$^{-3/2}$ (Vm^{-1}) are F–N constants, α is the field emission area, β is the field enhancement factor, Φ is the WF, d is the distance

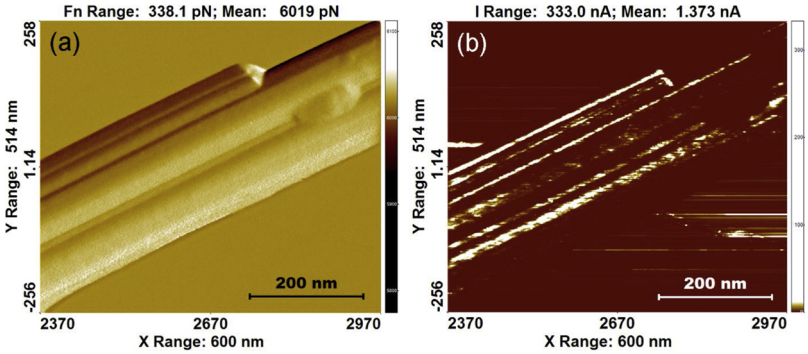

Fig. 7. Contact AFM observations of W_5O_{14} NW: a) topography image; b) current image.

between the anode and the apex of the NW and *V* is the applied voltage. The geometrical parameters mainly influencing the field enhancement factor are the ratio between the diameter and the length of the NW, the diameter of the nanowire, shape of the NW termination, the emitter-collector distance [26–28], etc.. Using Eq. 1, the field enhancement factor can be calculated from linear slope (*k*) of the F–N plot (log (I/V^2) vs. 1/V) [28]:

$$\beta = \frac{-Bd\Phi^{3/2}}{k}. \quad (2)$$

Considering an average work function of 4.3 eV for W_5O_{14} obtained from KPFM measurements, the apparent field enhancement factor for W_5O_{14} NW was 110 ± 10, 180 ± 25 and 210 ± 30 at 2, 4 and 5 μm, respectively. In comparison, the calculated field enhancement factor for $W_{18}O_{49}$ was 125 ± 15 at 2 μm, considering that the average WF is 4.56 eV. Larger field enhancement factor for $W_{18}O_{49}$ could be explained by protrusions (Fig. 8**b**-insert) or splinters (Fig. 4d) frequently observed at the ends of these NWs.

3.5. Field emission testing in macroscopic regime

The FE experiments at macroscopic distances (≈ 1 mm) were performed in two configurations: the $W_{18}O_{49}$ NW in a negatively biased cathode and grounded anode configuration [19], and W_5O_{14} NW in a positively biased electron extractor configuration [18].

3.5.1. Field emission from $W_{18}O_{49}$ wire

A $W_{18}O_{49}$ NW, 10 μm long and 180 nm in diameter, was attached on a tungsten electrochemically etched tip using FIB, as shown in the Fig. 12a. The I–V characteristics were measured with custom-made UHV system using a nanowire as an electron source and a Si wafer as an electron collector. The working pressure in the main chamber was 3.5×10^{-10} mbar.

Prior to field emission experiment, in-situ cleaning was performed by placing the tip in front of the first loop of a hot filament (~1500° C), which emitted electrons towards the positively biased tip (1 kV) shown in the Fig. 12b. The tip was annealed by the electron bombardment procedure for 15–20 min and flashed for 20 s. Typically, the annealing was performed at an emission current of 3–5 mA and flashing at a current of 20–30 mA.

After annealing, FE measurements of the $W_{18}O_{49}$ NW were carried out at two distances: 600 μm and 800 μm from the Si wafer. Fig. 13 shows the FE I–V characteristics for both distances and their corresponding F–N plots. At each position, FE experiments were performed three times in order to confirm repeatability. The FE currents were limited to 45 nA with the aim to prevent damage of the nanowire. The onset voltage of FE was 322 ± 1 V at 600 μm and 354 ± 1 V at 800 μm. The limit current was reached at 433 V and at 463 V, respectively (Fig. 13a). No significant differences were detected when the voltage was ramped up or down. In the F–N plots (Fig. 13b), the straight lines indicate the standard barrier-tunneling mechanism of the field electron emission. No degradation was observed.

The field enhancement factors were calculated according to the Fowler–Nordheim formalism for comparison with the relevant literature data. An average work function of $W_{18}O_{49}$ obtained from the KPFM measurements, i.e. 4.56 eV was considered. The field enhancement factors were 5050 ± 30 and 6450 ± 30 for 600 and 800 μm, respectively. These values were calculated using two parallel plates approximation, which is highly unrealistic for a nanowire emitter and flat electron collector at distances which, for several orders of magnitude, exceed the length of the nanowire. Therefore, a model developed for nanoemitters with an aspect ratio 1–500 and anode to cathode separation greater than three times the height of the emitter was used [29]:

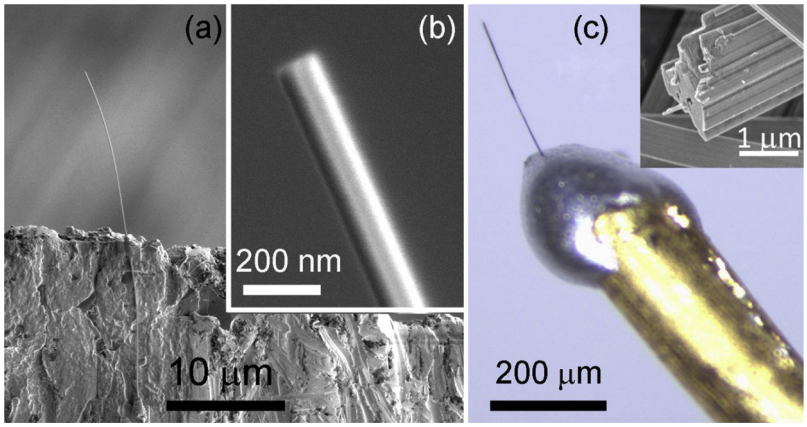

Fig. 8. SEM and optical images: a) W_5O_{14} nanowire on the W wire; b) rectangular termination of the W_5O_{14} NW; c) $W_{18}O_{49}$ wire on the Pt/Ir wire.

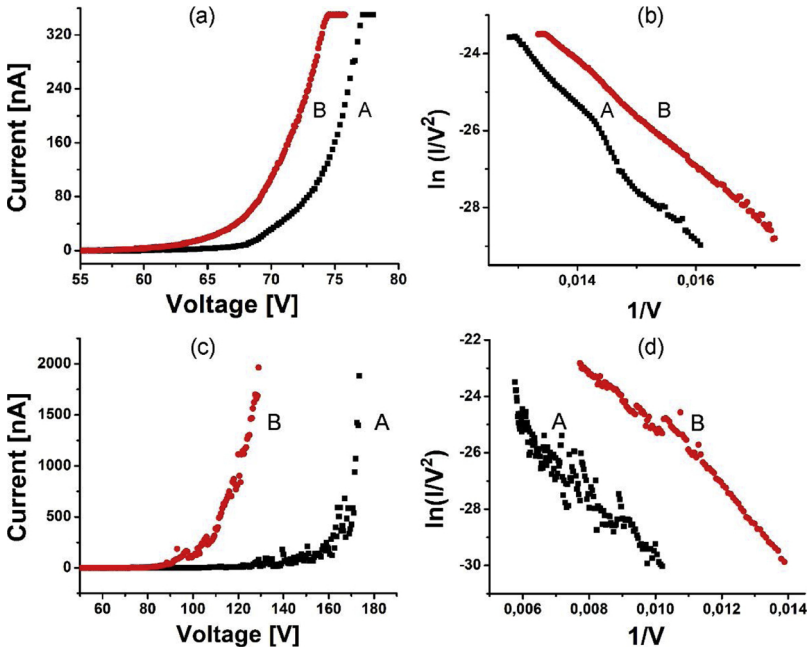

Fig. 9. I–V curves and corresponding F–N plots: a,b: W_5O_{14} NW ; c,d $W_{18}O_{49}$ wire. The first tests are labelled with A, and the second with B.

$$\beta = \left(1 + \sqrt{\frac{h}{\alpha r}}\right)^m \quad (3)$$

where h is length of the NW, r its radius, m = 1 and α = 2.

The field enhancement factor according to this model, which is independent on the anode location and is determined solely with length and diameter of an emitter, was 8 ± 0.5. Using this field enhancement factor, the onset fields for emission were 4.3 ± 0.3 V/μm and 3,5 ± 0.3 V/μm for 600 and 800 μm, respectively.

3.5.2. *Field emission from W_5O_{14} nanowire*

The W_5O_{14} NW used in the macroscopic FE regime measurement was 5 μm long, 148 nm in diameter (Fig. 14a) and mounted on an electrochemically etched tungsten wire by FIB. The experiment took place in an UHV chamber at 2×10^{-9} mbar with a separation of 1060 μm between the NW apex and the extractor plate.

Three relatively rough FE tests were performed. Voltage was manually increased step by step in 5 min intervals for the current to stabilize. In the first experiment, the voltage was increased to 990 V and the corresponding FE current reached 183 nA. The I–V curve (Fig. 14b) is exponential and relatively smooth. The second test revealed the maximum FE current of 1.2 μA at 890 V, while at higher voltages the current started to decrease. The FE current (990 nA) at 990 V was more than 5 times larger (Fig. 14c) than in the first test. In the third test, the maximum current of 1.063 μA was obtained at a higher voltage as in the second test, i.e. at 1063 V, while at 990 V the current was 1008 nA, i.e. again larger than in both previous tests (Fig. 14d). The explanation of the increase of FE current could be connected with the absence of cleaning of the emitters before FE testing. The subsequent tests gradually removed adsorbates from the NW, and the FE current consequently increased. Relatively high currents, which could cause diffusion of tungsten atoms and structural changes of the nanowire, could be the origin of degradation of the FE tip. While in the first test the maximum current was not reached, it decreased from the second to the third test for 12%. The onset voltages also increased gradually in subsequent tests, from 510 V, 535 V, to 551 V, respectively. Field enhancement factor from the F–N plot corresponding to the first test (Fig. 14e) was ≈ 17.000, while using the Eq. 3, it is 7 ± 0.5. The onset fields for three subsequent tests were 3.3 ± 0.3 V/μm, 3,4 ± 0.3 V/μ, and 3.5 ± 0.3 V/μm. The values match very well the onset field for emission from W_5O_{14} film [17].

4. Discussion

Two WO_{3-x} phases were studied, both in the shape of wires with a high aspect ratio. They differ in size, morphology, work function and field emission properties. In contrast with semiconducting WO_3 with a band gap in the range of 2.5–3.2 eV [9], the $W_{18}O_{49}$ and W_5O_{14} NWs are metallic with electrical resistance of 2750 μΩcm [12] and 25 μΩcm [7], respectively. The reason for improved electric conductance in these sub-stoichiometric WO_{3-x} phases are oxygen vacancies, which form

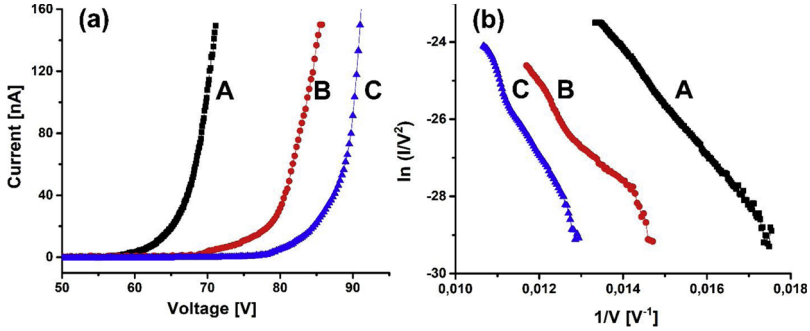

Fig. 10. I–V characteristics of a W_5O_{14} NW and the corresponding F–N plots. Distances between the NW tip and the electron collector: A - 2 μm; B - 4 μm; C - 5 μm.

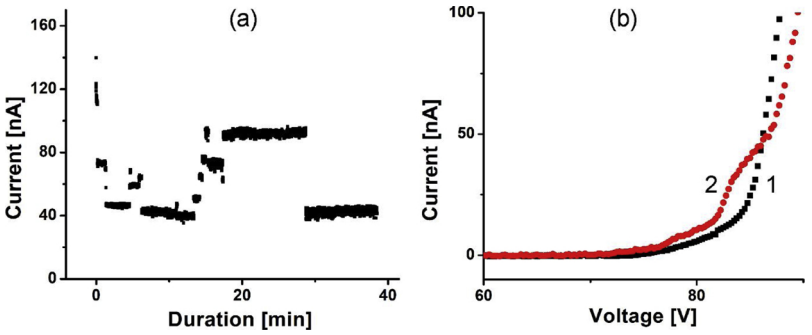

Fig. 11. a) FE current over time from a single W_5O_{14} NW, 5 μm away from electron collector, under 85 V of applied voltage; b) I–V curves before (1) and after (2) current time stability testing in total duration of 2,5 h under 80–85 V applied voltage.

donor states. Besides, these vacancies accumulate at the crystallographic shear planes, where they change the coordination number of tungsten ions from W^{+6} to W^{+5} [8] and cause structural changes like hexagonal or pentagonal tunnels in the structure oriented along the axis of the NWs [30]. Surface morphology of the NWs revealed by AFM and STM is not smooth, but wrinkled with undulations perpendicular to the NWs axis. These undulations can be understood as surface relaxation of the shear planes, which at the surface form undulated structure. The bottom parts of these undulations have the largest density of the oxygen vacancies, which is in accordance with the findings that they show the largest electric conductance in the current AFM image (Fig. 7) and the lowest work function (Figs. 5, 6). The same enhancement of electric conductance and decrease of work function was observed at longitudinal terminations of the NWs (Fig. 7), where the tunnels in the structure are exposed. Due to more than two orders of magnitude larger electric resistance of $W_{18}O_{49}$ NWs with respect to the W_5O_{14} NWs, and because of the diameter of W_5O_{14} is typically much smaller, the last ones were selected for detailed FE studies, and the former ones for comparison. While in-situ FE studies performed inside TEM from a single W_5O_{14} NW was reported with 35 μA extracted current [16], there is no report of FE studies on a single $W_{18}O_{49}$ NW, according to our knowledge. Our FE experiments were performed in ultra-high vacuum conditions at microscopic (2, 4, 5 μm) and macroscopic (600, 800, 1060 μm) distances between the tip of WO_{3-x} wires and the electron collectors. It was found, that at microscopic distances the field enhancement factors and onset voltages for FE increase with the distance, and two parallel plates model described by FN equation can be used. At 2 μm distance, there is no substantial difference in field enhancement factors between both types of the wires, i.e. 110 (W_5O_{14}) and 125 ($W_{18}O_{49}$), which could be explained with small splinters on otherwise wider $W_{18}O_{49}$ wires [30]. At the macroscopic distances, the FN equation revealed higher apparent field enhancement factors at the ends of W_5O_{14} NWs (17.000 at 1060 μm) than $W_{18}O_{49}$ NWs (5050 at 600 μm, and 6450 at 800 μm). This is explained with smaller diameter, deeper surface undulation, and the lower work function of W_5O_{14} NWs. The term "apparent" is used because the use of the FN equation in far field geometry is questionable and there is still an undergoing discussion, regarding the proper FE model in the far field geometry, within the scientific community. It represents an extreme ideal situation, which cannot be justified for our FE experiments done at macroscopic distances. Therefore, the other model [29] was utilized, which represent another extreme situation from the point that the field enhancement factor depends only on geometry of the emitter, i.e. its length and diameter. Using this model, the field enhancement factors are several orders of magnitude smaller than those calculated from FN equation. The values were: 8 ± 0.5 for $W_{18}O_{49}$ NW and 7 ± 0.5 for W_5O_{14} NW. This model predicts no dependency on cathode-anode distance, but our results do show the dependence of onset voltage and corresponding onset field on the distance between top of the emitter and electron collector. The onset fields for field emission (3–4 V/μm) match very well with the onset field for emission from W_5O_{14} film [17]. Nevertheless, it is worthy to note than neither of the above mentioned models cannot perfectly describe the results. It is known from other works, that the field enhancement factor increases by increasing the distance between the cathode and anode and by reducing the NW diameter [27,30]. In addition, the accurate emission area is not known. Reducing the diameter of the nanowires, the uncertainty of the emission area is also decreased, but special porous structure of the WO_x nanowires represents an additional challenge to find out, which part of the cross-section really emits. As it was shown in Fig. 6, the WF of the NW varies at the edge which could lead to field emission only from the part with the lowest WF. The apparent high field enhancement factors at macroscopic distances could be understood in a similar way as giant field enhancement up to 18 800 at carbon nanotubes grown on carbon cloth and explained by the multistage effect [31]. While the magnitude smaller nanotubes branching off the tips of bigger nanotubes were the

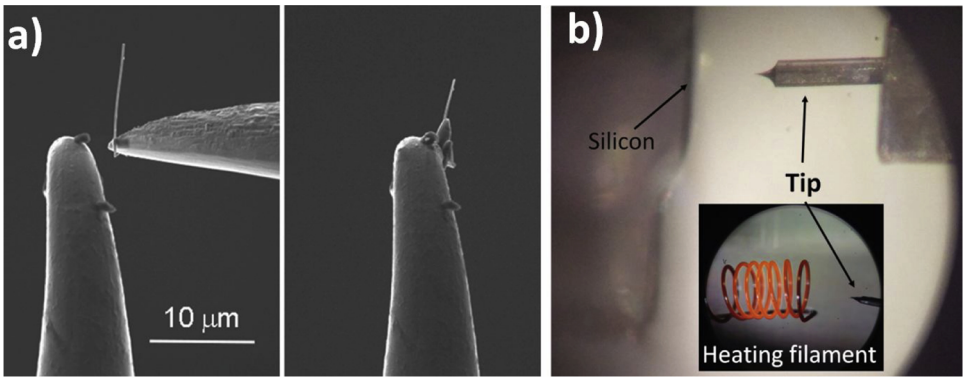

Fig. 12. a) SEM images showing the mounting of a single $W_{18}O_{49}$ NW; b) Optical image of the FE setup with the in-situ cleaning of the emitter by electron bombardment from heating filament.

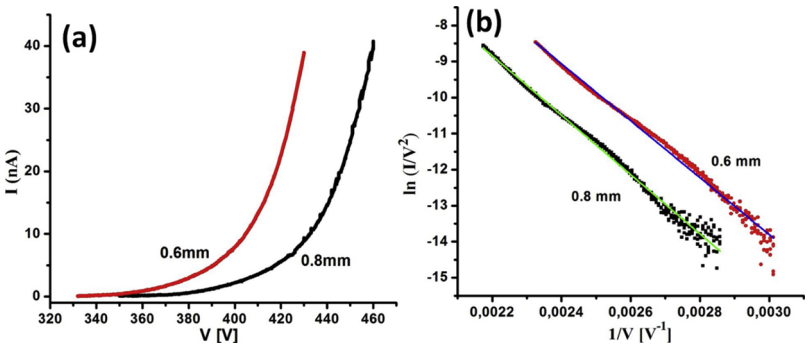

Fig. 13. FE testing of a $W_{18}O_{49}$ NW at two distances (600 μm and 800 μm): a) I–V characteristics; b) The corresponding F–N plots with linear fits.

origin of the field enhancement in carbon nanotubes case, the special porous structure of $W_{18}O_{49}$ wires and in particular W_5O_{14} NWs with deeper surface undulations could be the origin of the high field enhancement factors. One could assume that the areas around structural channels with concentrated oxygen vacancies and the bottom of the surface undulations with 50 mV lower work function than the average, represent the FE sites. Further research is needed to clarify this assumption.

5. Conclusion

In conclusion, field emission properties of single crystalline tungsten

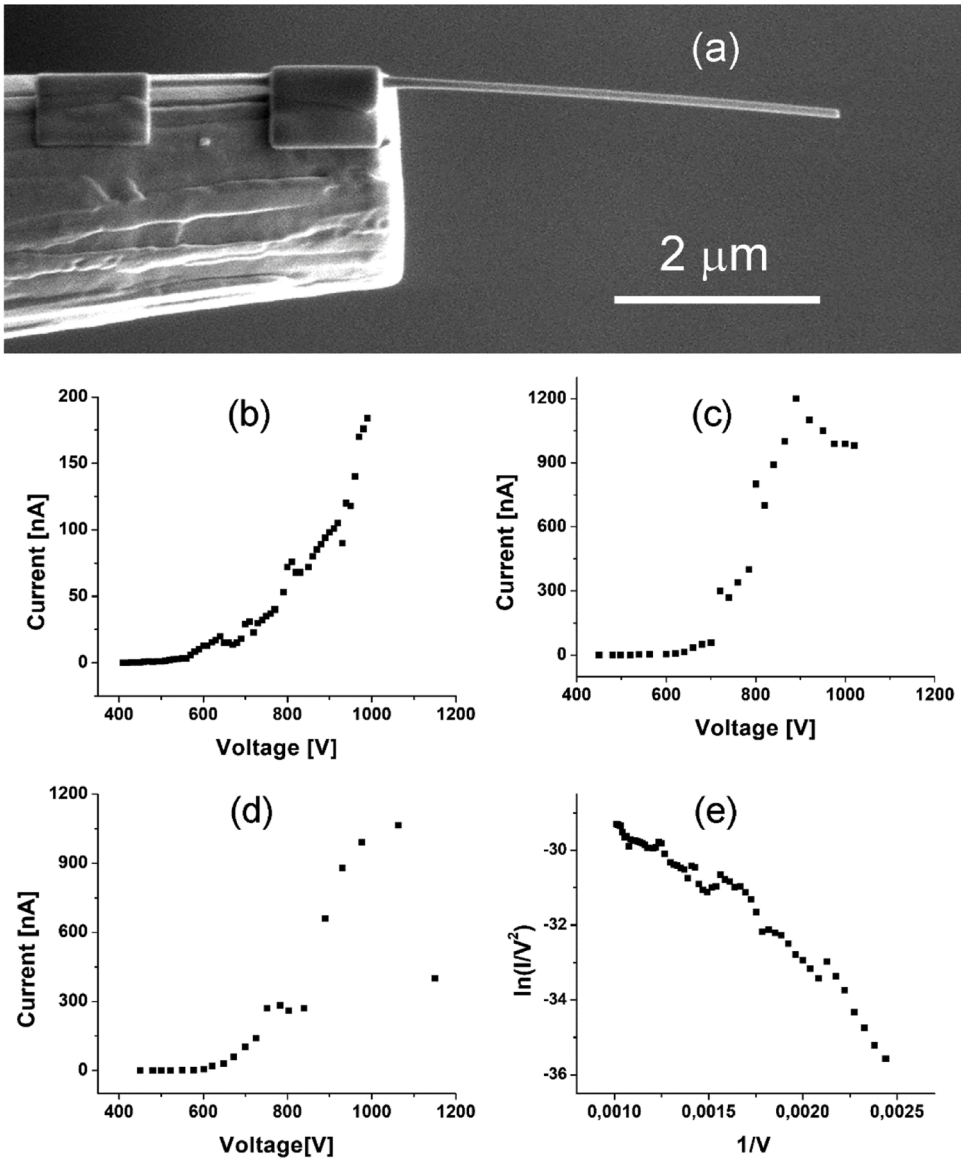

Fig. 14. a) SEM image of the W_5O_{14} NW mounted on tungsten wire; FE properties of a single W_5O_{14} NW in subsequent tests: b) the first test; c) the second test; d) the third test; e) F–N plot of the first test.

oxides W_5O_{14} and $W_{18}O_{49}$ wires were studied at microscopic and macroscopic distances between the nanowires and electron collectors. The work function of the NWs was determined by Kelvin probe force microscopy in non-contact AFM in ultrahigh vacuum. The average work function of W_5O_{14} NWs (4.3 eV) was found lower than $W_{18}O_{49}$ wires (4.56 eV), and the lowest, i.e. 4.2 eV inside surface corrugations of W_5O_{14}, where also enlarged electron conductance was observed with conductive AFM tip. The emitting characteristics of W_5O_{14} NWs situated at microscopic distances from electron collector follow the Fowler–Nordheim law with calculated field enhancement factors that are similar to the ones obtained from $W_{18}O_{49}$ NWs. It was found, that both the field enhancement factors and onset voltages increase with the distance between emitter and electron collector. At macroscopic distances, the Fowler–Nordheim formalism was used only for comparison with the literature data, while the results were explained with a model, which considers only the geometry of the nanowire in the calculation of the field enhancement factor. The onset fields were comparable for both kinds of the NWs. The obtained results open several perspectives in utilization of tungsten oxide nanowires as a source of low-energy electrons in different devices. In particular, the W_5O_{14} NWs are promising with larger electric conductance and typically smaller diameter than $W_{18}O_{49}$ NWs, as well as due to relatively high field enhancement factors they can be activated at relatively low electric fields.

Acknowledgment

This research was financially supported by the SIMDALEE2-Sources, Interaction with Matter, Detection, and Analysis of Low Energy Electrons, a Marie Curie Initial Training Network (Grant No. PITN 606988), financed by the European Commission. The first author (M.S.) is thankful for the financial support form ETH Zurich and to Prof. Danilo Pescia and his research group for help in experiments. We acknowledge Slovenian Research Agency for co-financing. The research was also funded by the Technology Agency of the Czech Republic, Project No. TE01020118.

References

[1] K. Gesheva, T. Ivanova, G. Bodurov, I.M. Szilágyi, N. Justh, O. Kéri, S. Boyadjiev, D. Nagy, M. Aleksandrova, Technologies for deposition of transition metal oxide thin films: application as functional layers in “Smart windows” and photocatalytic systems, J. Phys: Conf Ser. 682 (1) (2016) 012011 IOP Publishing.
[2] B. Gavanier, F.M. Michalak, J.R. Owen, Electrochemistry of WO 3 based smart windows: beliefs and facts, Ionics 3 (May (3-4)) (1997) 265–269.
[3] M. Ladouceur, J.P. Dodelet, G. Tourillon, L. Parent, S. Dallaire, Plasma-sprayed semiconductor electrodes: photoelectrochemical characterization and ammonia photoproduction by substoichiometric tungsten oxides, J. Phys. Chem. 94 (May (11)) (1990) 4579–4587.
[4] Z.F. Huang, J. Song, L. Pan, X. Zhang, L. Wang, J.J. Zou, Tungsten oxides for photocatalysis, electrochemistry, and phototherapy, Adv. Mater. 27 (September (36)) (2015) 5309–5327.
[5] K.R. Locherer, I.P. Swainson, E.K. Salje, Phase transitions in tungsten trioxide at high temperatures-a new look, J. Phys. Condens. Matter 11 (September (35)) (1999) 6737.
[6] I.J. McColm, R. Steadman, S.J. Wilson, Iron-promoted phases in the tungsten-oxygen system, J. Solid State Chem. 23 (January (1-2)) (1978) 33–42.
[7] M. Remškar, J. Kovac, M. Viršek, M. Mrak, A. Jesih, A. Seabaugh, W5O14 nanowires, Adv. Funct. Mater. 17 (August (12)) (2007) 1974–1978.
[8] M. Sundberg, R.J. Tilley, An electron microscope study of some nonstoichiometric tungsten oxides, J. Solid State Chem. 11 (October (2)) (1974) 150–160.
[9] F. Wang, C. Di Valentin, G. Pacchioni, Electronic and structural properties of WO3: a systematic hybrid DFT study, J. Phys. Chem. C 115 (April (16)) (2011) 8345–8353.
[10] T. Hirose, I. Kawano, M. Niino, Electrical conductivity of tungsten trioxide (WO3), J. Phys. Soc. Jpn. 33 (July (1)) (1972) 272.
[11] Z. Hu, Z. Ji, W.W. Lim, B. Mukherjee, C. Zhou, E.S. Tok, C.H. Sow, K-enriched WO3 nanobundles: high electrical conductivity and photocurrent with controlled polarity, ACS Appl. Mater. Interfaces 5 (May (11)) (2013) 4731–4738.
[12] K. Viswanathan, K. Brandt, E. Salje, Crystal structure and charge carrier concentration of W18O49, J. Solid State Chem. 36 (January (1)) (1981) 45–51.
[13] W.Q. Chen, R.Z. Zhan, S.Z. Deng, N.S. Xu, J. Chen, Anomalous temperature dependence of field emission from W18O49 nanowires caused by surface states and field penetration, J. Appl. Phys. 116 (January (13)) (2014) 133506.
[14] J. Zhou, L. Gong, S.Z. Deng, J. Chen, J.C. She, N.S. Xu, R. Yang, Z.L. Wang, Appl. Phys. Lett. 87 (November (22)) (2005) 223108.
[15] W.Q. Chen, C.X. Zhao, J.Q. Wu, S.Z. Deng, N.S. Xu, J. Chen, Phonon-assisted field emission from W18O49 nanowires, Appl. Phys. Lett. 103 (September (14)) (2013) 141915.
[16] M. Žumer, V. Nemanič, B. Zajec, M. Wang, J. Wang, Y. Liu, L.M. Peng, The field-emission and current− voltage characteristics of individual W5O14 nanowires, J. Phys. Chem. C 112 (April (14)) (2008) 5250–5253.
[17] G. Ulisse, C. Ciceroni, A.D. Carlo, F. Brunetti, J. Jelenc, M. Saqib, A. Varlec, M. Remskar, Synthesis and field emission characteristics of W5O14 nanowires film, Microelectron. Eng. 25 (February 170) (2017) 44–48.
[18] A. Knápek, L. Grmela, Methods of Preparation and Characterisation of Experimental Field-emission Cathodes, Vysoké učení technické, 2013.
[19] De Pietro L.G. Field Emission Scanning Tunnelling Microscopy with Spin Polarisation Analysis (Doctoral dissertation, ETH Zurich).
[20] J. Booth, T. Ekström, E. Iguchi, R.J. Tilley, Notes on phases occurring in the binary tungsten-oxygen system, J. Solid State Chem. 41 (March (3)) (1982) 293–307.
[21] Y. Li, Y. Bando, D. Golberg, Quasi-Aligned Single-Crystalline W18O49 Nanotubes and Nanowires, Adv. Mater. 15 (August (15)) (2003) 1294–1296.
[22] M. Nonnenmacher, M.P. o'Boyle, H.K. Wickramasinghe, Kelvin probe force microscopy, Appl. Phys. Lett. 58 (June (25)) (1991) 2921–2923.
[23] T. Glatzel, S. Sadewasser, M.C. Lux-Steiner, Amplitude or frequency modulation-detection in Kelvin probe force microscopy, Appl. Surf. Sci. 210 (March (1-2)) (2003) 84–89.
[24] F. Maeda, T. Takahashi, H. Ohsawa, S. Suzuki, H. Suematsu, Unoccupied-electronic-band structure of graphite studied by angle-resolved secondary-electron emission and inverse photoemission, Phys. Rev. B 37 (March (9)) (1988) 4482.
[25] K.A. Dean, B.R. Chalamala, Current saturation mechanisms in carbon nanotube field emitters, Appl. Phys. Lett. 76 (January (3)) (2000) 375–377.
[26] R.C. Smith, S.R. Silva, Interpretation of the field enhancement factor for electron emission from carbon nanotubes, J. Appl. Phys. 106 (July (1)) (2009) 014314.
[27] R.C. Smith, D.C. Cox, S.R. Silva, Electron field emission from a single carbon nanotube: effects of anode location, Appl. Phys. Lett. 87 (September (10)) (2005) 103112.
[28] H. Liu, S. Kato, Y. Saito, Effect of cathode-anode distance on field emission properties for carbon nanotube film emitters, Jpn. J. Appl. Phys. 20 (January 48) (2009) 015007.
[29] R.C. Smith, J.D. Carey, R.D. Forrest, S.R.P. Silva, Effect of aspect ratio and anode location on the field emission properties of a single tip based emitter, J. Vac. Sci. Technol. B 23 (2005) 632.
[30] G.L. Frey, A. Rothschild, J. Sloan, R. Rosentsveig, R. Popovitz-Biro, R. Tenne, Investigations of nonstoichiometric tungsten oxide nanoparticles, J. Solid State Chem. 162 (December (2)) (2001) 300–314.
[31] J.Y. Huang, K. Kempa, S.H. Jo, S. Chen, Z.F. Ren, Giant field enhancement at carbon nanotube tips induced by multistage effect, Appl. Phys. Lett. 87 (August (5)) (2005) 053110.
[32] E. Sergeev, et al., Noise diagnostic method of experimental cold field-emission cathodes, 2013 22nd International Conference on Noise and Fluctuations (ICNF) (2013) 1–4.